PAPER

Peptide-templated synthesis of branched MnO₂ nanowires with improved electrochemical performances†

Mingxuan Du,[a] Yong Bu,[a] Yan Zhou,[b] Yurong Zhao,[a] Shengjie Wang*[a] and Hai Xu*[a]

Although many nanomaterials have been prepared *in vitro* by mimicking biomineralization, the biomimetic synthesis of hybrids with both well-ordered nanostructures and specific functions is still in its infancy. A short designed peptide amphiphile I₃K can form uniform and stable nanofibers in aqueous solution, with a surface enriched in cationic lysine residue. In the present study, we have demonstrated that the peptide nanofibers could direct the synthesis of MnO₂ nanowires under mild conditions. By varying the concentration of manganese precursors (KMnO₄ and Mn(NO₃)₂), uniform branched MnO₂/peptide hybrid nanowires with high porosity and a large specific surface area were obtained. The well-defined MnO₂ hybrid nanowires showed significantly improved electrochemical supercapacitive properties relative to compact MnO₂ nanowires and urchin-like MnO₂ spheres. Their specific capacitance could attain a higher value of 421 F g⁻¹ and retained about 93% of the initial capacitance after 2500 cycles at a scan rate of 5 mV s⁻¹, and remained little changed during the process of progressively varying the current density. Furthermore, the electrode prepared from the uniform MnO₂ hybrid nanowires showed an excellent reversibility and a reasonably high-rate capability during the charge/discharge process. Such a study provides a new methodology to prepare functional MnO₂ nanostructures under mild conditions that can be used in electrochemical energy storage.

Introduction

Supercapacitors have attracted great attention as electrochemical energy storage devices and exhibited potential applications in hybrid electric vehicles, sensors-actuators, uninterruptable power suppliers, and energy-harvesting systems because of their high power density, rapid charge/discharge rate, temperature stability and long cycling life.[1] According to their different charge-storage mechanisms, supercapacitors can be classified into two groups, *i.e.*, double-layer capacitors and pseudo-capacitors.[1,2] Compared with the double-layer capacitor in which charge storage merely occurs on the electrode surface, the pseudo-capacitor has higher specific capacitance due to the electrochemical transformation both in the bulk phase and on the surface of electrodes. Pseudo-capacitors that use conducting polymers[3–5] or transition metal oxides[6–9] as electrode materials rely on redox reactions between these electroactive materials and ions in electrolytes. Metal oxides, such as MnO₂, NiO, RuO₂, and V₂O₅ are of particular interest due to their high energy density, multiple and variable oxidation state, and excellent stability during the faradaic reaction.[2,6–9] Among them, MnO₂ has exhibited many advantages such as high theoretical specific capacitance, low cost and toxicity, nature abundance, and easy preparation, and as a result, it has been widely exploited as one of the most promising electrode materials for pseudo-capacitors.[1,2]

However, the poor electric conductivity and the low accessible surface areas of thick MnO₂ often limit the specific capacitance of conventional MnO₂ electrodes of only 150–250 F g⁻¹, which is far from the theoretical value of ∼1370 F g⁻¹.[2,10–12] Correspondingly, there are currently two strategies to improve the electrochemical capacitance properties of MnO₂.[2] One is to increase the electrical conductivity of MnO₂ electrodes by incorporation of other metal or carbon materials. The other one is to increase the specific surface area and regulate the pore size distribution of MnO₂. It is well-known that nanostructured materials usually have high specific surface areas. Thus, different manganese oxide nanostructures such as nanoparticles, nanorods, nanowires, nanoplates, and nanoflowers have been synthesized and their electrochemical capacitance performances were found to be close correlated to the morphologies, surface areas, and pore sizes and distributions.[13–16]

In order to obtain MnO₂ nanomaterials, many methods such as sol–gel transition, hydrothermal synthesis, electrochemical deposition, and template-assisted anodic electrodeposition have been exploited.[13–20] To further increase their specific

[a]State Key Laboratory of Heavy Oil Processing and Center for Bioengineering and Biotechnology, China University of Petroleum (East China), No. 66 Changjiang West Road, Qingdao 266580, China. E-mail: sjwang@upc.edu.cn; xuh@upc.edu.cn; Tel: +86-532-86981569

[b]College of Science, China University of Petroleum (East China), No. 66 Changjiang West Road, Qingdao 266580, China

† Electronic supplementary information (ESI) available. See DOI: 10.1039/c7ra00829e

surface areas and simultaneously to avoid the use of special equipment and harsh conditions during synthesis, however, there are still urgent demands for new synthetic strategies that work under mild conditions. Inspired by biomineralization and biomimetic synthesis of well-defined nanostructures,[21,22] we here constructed novel MnO_2 nanostructures under mild conditions by taking advantage of peptide self-assembly. The used peptide I_3K is a designed short amphiphile, three consecutive Ile residues constituting the hydrophobic tail and one positively charged Lys acting as the hydrophilic head (Fig. S1†).[23,24] In aqueous solutions, the peptide can readily self-assemble into uniform and stable nanofibers, and because their surface is enriched in cationic lysine residues, silica nanotubes have been successfully templated.[23,25,26] In this case, the I_3K nanofibers were found to direct the deposition of MnO_2 that arose from the comproportionation reaction between $KMnO_4$ and $Mn(NO_3)_2$ in neutral water at room temperature, resulting in the formation of MnO_2 nanowires. The templating ability of the peptide nanofibers arose from their surface lysine residues and by varying the concentrations of manganese precursors, MnO_2 nanowires with different morphologies could be obtained. The uniform branched MnO_2 nanowires had a porous structure with a high specific surface area up to 275 m^2 g^{-1}, and importantly, they showed significantly improved electrochemical properties, relative to compact MnO_2 nanowires and the urchin-like MnO_2 nanospheres formed in the absence of peptide. Such a study provides a simple biomimetic method to obtain MnO_2 electrode nanomaterials with excellent electrochemical performances.

Materials and methods

Materials

The peptide I_3K was synthesized on a CEM Liberty microwave synthesizer according to Fmoc solid-phase chemistry. The use of Rink amide MBHA resin made its C-terminus amidation while its N-terminus was capped with acetic anhydride before cleavage from the resin. The detailed synthesis and purification procedures have been given in our previous publications.[23,24] All the materials used for peptide synthesis were purchased from GL Biochem Ltd (Shanghai, China). $KMnO_4$, $Mn(NO_3)_2$, and other reagents were obtained from Sigma-Aldrich and used as received. All water used was obtained from a Millipore water purification system with a minimum resistivity of 18.2 MΩ cm.

Peptide self-assembly

I_3K showed high solubility in aqueous solutions. After dissolving the peptide in ultrapure water to obtain a clear peptide solution of 4 mM, the solution pH was slightly adjusted to 7.0 using dilute NaOH solution. The peptide solution was kept at room temperature for at least one week before instrumental characterizations and use in mineralization.

Preparation of MnO_2 nanomaterials

MnO_2 was synthesized *via* the redox reaction between $KMnO_4$ and $Mn(NO_3)_2$ in the presence and absence of I_3K assemblies. By varying the concentrations of $KMnO_4$ and $Mn(NO_3)_2$, different MnO_2 nanomaterials were obtained. Taking the synthesis of MP-5 as an example (as indicated in Table 1), 1 mL of the aged I_3K solution (4 mM) was mixed with 2.8 mL of ultrapure water, 0.2 mL of 0.1 M $KMnO_4$ aqueous solution, and 0.01 mL of 4 M $Mn(NO_3)_2$ aqueous solution, and the final concentration of I_3K, $KMnO_4$, and $Mn(NO_3)_2$ in the mixture was 1, 5, and 10 mM, respectively. After mixing, brown precipitates were immediately observed, indicating that the reaction was fast. In spite of this feature, the mixture was kept for 24 hours at room temperature to ensure a complete reaction. To remove residual precursors, the above reaction solution was centrifuged at 10 000 rpm for 10 min, and the precipitate was washed alternately with water and ethanol for three times, followed by freeze-drying overnight. Finally, loose powders of MnO_2/peptide hybrid were collected for subsequent characterizations.

Preparation of MnO_2 electrodes

The working electrodes were prepared using Ni foam as a current collector (1.0×1.0 cm^2). The Ni foam was first cleaned successively with ethanol and ultra-pure water to remove

Table 1 Synthesis conditions for different MnO_2 nanostructures and their morphologies and specific capacitances

Name of MnO_2	Concentration (mM)			Morphology	Specific capacitance^a (F g^{-1})
	I_3K	$KMnO_4$	$Mn(NO_3)_2$		
MP-0	0	5	10	Urchin-like sphere	194
MP-1	1	0.1	0.2	Thin and compact nanowire	124
MP-2	1	0.2	0.4	Thin and compact nanowire	139
MP-3	1	1	2	Thin and compact nanowire	163
MP-4	1	2	4	Rough nanowire	194
MP-5	1	5	10	Uniform branched nanowire	421
MP-6	1	10	20	Branched nanowire (main), urchin-like sphere	313
MP-7	1	20	40	Urchin-like sphere (main), branched nanowire	226

^{a} The specific capacitance of MnO_2 nanomaterials was calculated from their CV curves at 5 mV s^{-1}, according to the eqn (1).

residual organics. Then, nanostructured MnO_2, acetylene black, and polytetrafluoroethylene were well mixed in ethanol at a mass ratio of 80 : 15 : 5 and dried under vacuum at 60 °C for 12 h. After loading the mixed powder onto the Ni foam, the electrode was obtained by pressing the foam under a pressure of 10 MPa.

Instrumental characterizations

XRD. An X Pert PRO MPD X-ray diffractometer (Cu Kα, λ = 0.154 nm, 45 kV, 50 mA) was used to follow the crystallographic characteristic of MnO_2 nanomaterials. The diffractometer was operated at 45 kV and 50 mA at a step of $2°$ min^{-1}.

TEM. Conventional transmission electron microscopy (TEM) measurements were performed on a JEOL JEM-1400plus electron microscope operated with an accelerating voltage of 120 kV. High-revolution TEM (HR-TEM) images and the selected area electron diffraction (SAED) pattern were obtained on a JEOL JEM-2100UHR instrument operated at 200 kV. MnO_2 nanomaterials were dispersed in ethanol and directly pipetted on a copper grid covered with a carbon film, and no staining agent was applied for subsequent observation. As for the samples only containing peptide, after the peptide solution was deposited onto a copper grid covered with a carbon film, they were negatively stained with 2% uranyl acetate for subsequent TEM observation.

XPS. X-ray photoelectron spectra (XPS) were recorded on a Thermo ESCALAB 250 electron spectrometer with a monochromatic Al Kα X-ray source (photon energy $hν$ = 1486.6 eV) operated at 150 W with a spot size of ~500 μm. The spectrometer was calibrated using the C 1s peak at 284.6 eV. The overlapped XPS peaks were deconvoluted and fitted with Gaussian peaks after subtraction of a Shirley background.

BET. The specific surface area of MnO_2 nanomaterials was assessed by a Brunauer–Emmett–Teller (BET) technique on a Quantachrome Autosorb-6B instrument after degassing overnight at approximately 200 °C. The pore size distribution was analyzed based on slit-like pore geometry.[27]

FTIR. Fourier transform infrared spectroscopy (FTIR) measurements were conducted on a Nicolet 6700 FT-IR spectrometer, using thin KBr slices as the sample holder. The scanning range was set from 4000 to 400 cm^{-1} with a resolution of 4 cm^{-1}.

Electrochemical properties. The electrochemical characteristics of MnO_2 nanomaterials were carried out using a three-electrode experimental setup on a CHI660D electrochemical workstation (CH Instrument, Shanghai), in which a platinum wire and a saturated calomel electrode (SCE) were used as the counter and reference electrode, respectively. The electrolyte was an aqueous solution of 1 M Na_2SO_4 for all the measurements.

Results and discussion

Preparation of branched MnO_2 nanowires

As demonstrated previously, I_3K nanofibers could template the formation of long silica nanotubes.[23,25] The underlying

mechanism was related to the lysine residues distributed on the I_3K nanofibers' surface and there was an electrostatic attraction between silica intermediates and the surface lysine residues at around neutral pH. By taking advantage of this nanostructured peptide template with a well-defined surface chemistry, we here realized the template synthesis of MnO_2 nanomaterials with ordered architectures under mild conditions.

Manganese oxide (MnO_2) was prepared *via* the comproportionation reaction between $KMnO_4$ and $Mn(NO_3)_2$ in neutral water at room temperature, which is as the following:

$$2MnO_4^- + 3Mn^{2+} + 2H_2O \rightarrow 5MnO_2 + 4H^+$$
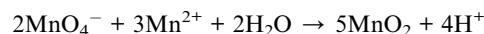
In our experiment, the molar ratio of $KMnO_4$ and $Mn(NO_3)_2$ was set as 1 : 2, which was slightly lower than their stoichiometric ratio (2 : 3), thus allowing the powerful oxidizing agent ($KMnO_4$) to react completely. In the absence of peptide, the collected brown precipitates showed an urchin-like morphology with diameters mostly ranging from 140 to 260 nm (Fig. S2a in ESI†), and it can be seen from a HR-TEM micrograph that the urchin-like structure was assembled from many thin MnO_2 nanoflakes (Fig. S2b†).

I_3K self-assembled into long nanofibers with diameters of 10.5 ± 3 nm (Fig. S1b†). In the presence of I_3K, we also observed brown precipitates immediately after mixing the aged peptide solution with $KMnO_4$ and $Mn(NO_3)_2$. After 24 h, however, the collected precipitates showed complete different morphologies from that formed in the absence of peptide. As shown in Fig. 1 and Table 1, we observed the deposition of MnO_2 along the peptide nanofibers, resulting in the formation of fiber-like precipitates with a high aspect ratio. Such a peptide-templated synthesis was first verified by FTIR analysis, in which the characteristic bands of both amide and manganese oxide were observed from the collected fiber-like precipitates (Fig. S3†). With increasing the concentration of manganese precursors whilst keeping their molar ratio being constant ($KMnO_4$: $Mn(NO_3)_2$, 1 : 2), the coating of manganese oxides on the peptide fibers showed increases in thickness, surface
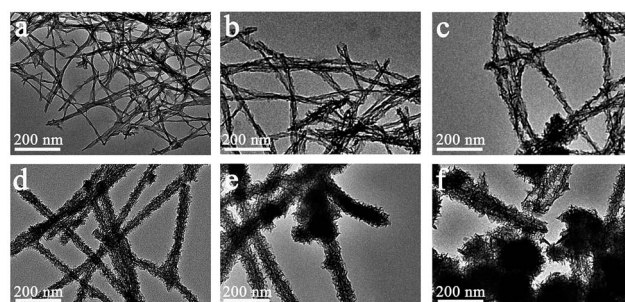

Fig. 1 TEM micrographs of representative MnO_2 nano-structures formed in the presence of I_3K nanofibers: (a) MP-2 (0.6 mM manganese precursors, similarly hereinafter), (b) MP-3 (3 mM), (c) MP-4 (6 mM), (d) MP-5 (15 mM), (e) MP-6 (30 mM), (f) MP-7 (60 mM). The peptide concentration was fixed as 1 mM. The molar ratio of $KMnO_4$ and $Mn(NO_3)_2$ was fixed as 1 : 2 while their total concentration was changed, as indicated in Table 1.

RSC Advances

Paper

roughness and even morphology (Fig. 1 and S4†). For instance, the fiber-like precipitates (MP-2 and MP-3) showed a compact MnO_2 layer, with a diameter of 14.1 ± 6 and 22.4 ± 12 nm at a precursor concentration of 0.6 and 3 mM, respectively (Fig. 1a and b and S4a and b†). At a precursor concentration of 6 mM, the diameter was increased to 29.3 ± 8 nm and importantly, the assembly of some thin MnO_2 nanoflakes along the peptide template occurred, resulting in a rougher surface morphology (MP-4, Fig. 1c and S4c†). As the precursor concentration was increased to 15 mM, the peptide nanofibers were totally covered by thin MnO_2 nanoflakes, leading to the formation of uniform branched MnO_2/peptide hybrid nanowires (MP-5, Fig. 1d and 3a). In this case, the diameter of inorganic coatings was increased to 42.4 ± 11 nm (Fig. S4d†). With further increasing the precursor concentration to 30 mM, we observed the occurrence of spherical urchin-like MnO_2 nanostructures, which were similar to that formed in the absence of peptide, in addition to dominant branched MnO_2 hybrid nanowires with a diameter of 51.3 ± 10 nm (Fig. 1e and S4e†). At a much higher precursor concentration of 60 mM, free urchin-like MnO_2 spheres dominated while branched MnO_2 hybrid nanowires remained little change in their diameters (Fig. 1f and S4f†). These results suggest that the templating ability of the peptide fibers has been saturated at higher concentrations of manganese precursors, thus leading to the random deposition of spherical urchin-like MnO_2 (Fig. 1e and f).

At a precursor concentration of 15 mM, the formed MnO_2 hybrid (MP-5) showed the most uniform branched nanowire morphology without randomly deposited urchin-like MnO_2 spheres and importantly, the sample displayed the best electrochemical properties, as indicated below. Thus, further compositional and structural assessments were focused on the sample. First, the signals of Mn 2p, O 1s, N 1s, and C 1s were clearly observed in the XPS survey spectrum of MP-5 (Fig. 2a). Second, the high-resolution spectrum of Mn 2p indicated two peaks centered at 642.2 and 653.9 eV, which were attributed to Mn $2p_{3/2}$ and Mn $2p_{1/2}$, respectively. The peaks values and

a spin-energy separation of 11.7 eV were well consistent with the reported data of Mn $2p_{3/2}$ and Mn $2p_{1/2}$ of MnO_2.[28–32] Third, as reported by Toupin et al. and Chigane et al., the energy separation between the two weak peaks of Mn 3s is 5.41 and 4.78 eV for Mn^{3+} and Mn^{4+} oxides, respectively, and a low valence of Mn usually results in a wider splitting of the two Mn 3s peaks.[11,33] In this case, the observed value of 4.85 eV was close to that of Mn^{4+} oxide (4.78 eV) (Fig. 3c). These results suggest the overwhelming predominance of the +4 oxidation state for the manganese oxide deposited along the peptide nanofibers. On the other hand, the slight increase in the Mn 3s energy separation from 4.78 to 4.85 eV was likely to be caused by minor Mn^{3+} in the deposited MnO_2. In fact, it has been reported that some surface Mn^{3+} (reactive intermediate) remained unoxidized during oxidative precipitation of MnO_2 from Mn^{2+}-bearing aqueous solutions.[34] The deconvolution of the O 1s spectrum produced a major peak at 529.9 and a minor one on its high binding energy side (531.4 eV), the former corresponding to the Mn–O–Mn bond for the tetravalent oxide while the latter being likely ascribed to the combined effect of the Mn–OH bond for a hydrated trivalent oxide and the H–O–H bond for residual structure water (Fig. 2d).[11,34] Thermal gravimetric analysis (TGA) indicated about 10 wt% of residual water in the sample (Fig. S5†).

High-magnification TEM images clearly indicated that the branched MnO_2 nanowires arose from the assembly of small and ultrathin MnO_2 nanoflakes along the peptide template (Fig. 3a), and in some cases, the peptide nanofibers were still discernible (red arrows in Fig. 3a). The small nanoflakes were uniformly distributed on the template surface and well interconnected, and their thickness was estimated to be less than 5 nm by measuring the width of black lines (insets of Fig. 3a). HR-TEM characterization showed that the edge of the MnO_2 nanoflakes was highly transparent (Fig. 3b), being consistent with their ultrathin thickness. Importantly, HR-TEM and SAED investigations indicated that the branched MnO_2 nanostructures had low crystallinity (Fig. 3b and c). In spite of their weak crystalline property, some crystallizing micro-zones in the HR-TEM micrograph revealed a d-spacing of 0.69 nm, being
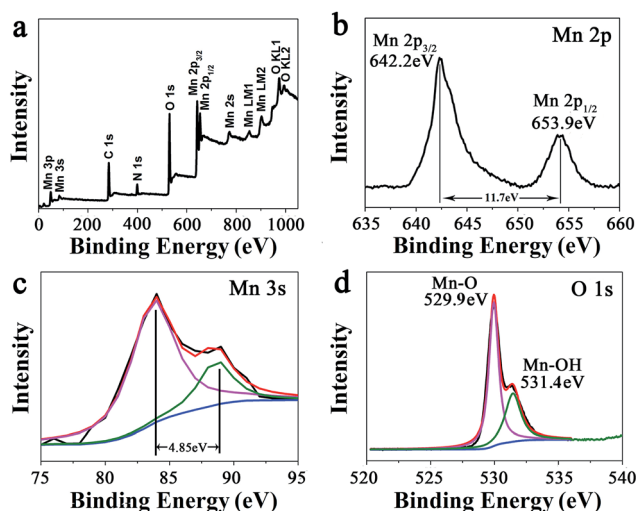

Fig. 2 (a) XPS survey spectrum of branched MnO_2 nanowires (MP-5) and the narrow XPS spectra of (b) Mn 2p, (c) Mn 3s, and (d) O 1s of MP-5.
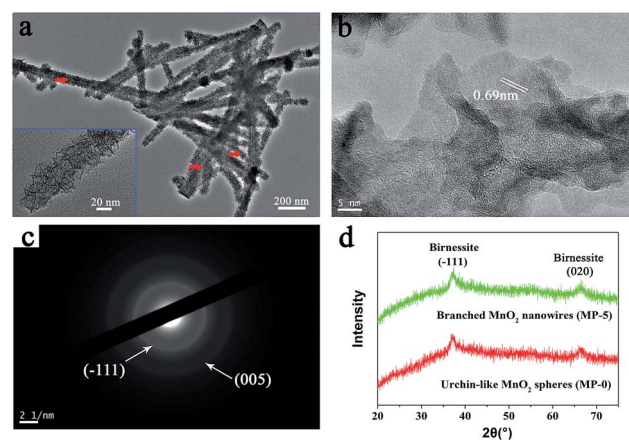

Fig. 3 (a) High-magnification TEM image, (b) HR-TEM image, and (c) SAED pattern of branched MnO_2 nanowires (MP-5). (d) XRD patterns of MP-5 and MP-0 (urchin-like MnO_2 spheres).

consistent with the interplanar spacing of the (001) plane of birnessite-type MnO_2.[27,30,35,36] Additionally, X-ray diffraction (XRD) measurements only revealed two weak diffraction peaks for the branched MnO_2 nanowires as well as the urchin-like MnO_2 spheres, indicating their poor crystallinity (Fig. 3d). The two peaks can be indexed to the (−111) and (020) planes of birnessite-type MnO_2 (JCPDS 80-1098). The poor crystallinity of these inorganic nanostructures may be attributed to that the comproportionation reaction rate was too fast to enable well-ordered arrangement during the MnO_2 precipitation, as observed in the preparation of core-corona hierarchical MnO_2 nanostructures.[35] Overall, the results of XPS, TEM, and XRD indicated that the peptide nanofibers mainly directed the morphology and nanostructure of MnO_2 precipitates while had little influence on their crystalline nature.

Because the branched MnO_2 nanowires were formed through the assembly of numerous small and ultrathin flakes directed by the peptide nanofibers, a large surface area and a porous feature would thus be expected. As shown in Fig. 4a, the N_2 adsorption/desorption measurement of MP-5 showed a typical IV-type isotherm with a hysteresis loop in a relative pressure (p/p_0) range of 0.4 to 1.0, being consistent with the disordered mesoporous materials.[27,28,37] The BET surface area of the branched MnO_2 nanowires (MP-5) was calculated to be 275 m^2 g^{-1}, which was much higher than that (187 m^2 g^{-1}) of urchin-like MnO_2 spheres and those of previously reported hybrid nanostructures such as MnO_2/SiNWs and MWCNTs@MnO_2.[27,37] The Barett–Joyner–Halenda (BJH) pore size distribution curve of MP-5 was given in Fig. 4b. A distribution ranging from 3 to 8 nm with a distinct maximum centered at 5 nm was observed. These mesopores corresponded to slit-like pores, as a result of the stacking of numerous small and ultrathin MnO_2 nanoflakes.[27] The high specific surface area and the mesoporous nature of the branched MnO_2 nanowires (MP-5) not only provided more surface active sites for electrochemical reactions but also favored the transport of both electrons and cations (shortening their transport path length), thus most likely endowing them with high specific capacitance. In contrast, the urchin-like MnO_2 spheres (MP-0) formed in the absence of peptide has a significantly decreased surface area (187 m^2 g^{-1}) and a narrower pore sized distribution with a much smaller maximum centered at 3 nm (Fig. S6†), indicating a dense packing of MnO_2 nanoflakes in this case.

Although $KMnO_4$ is a strong oxidant and many studies have utilized the redox reaction between $KMnO_4$ and carbon (e.g.

carbon nanotubes and graphene) to prepare supercapacitor electrode materials without any reductant addition under acidic and/or hydrothermal conditions,[10,29,30,38–40] there was little redox reaction between $KMnO_4$ and I_3K in our case (neutral pH and room temperature), which was confirmed by the XPS analysis on the collected MnO_2/peptide hybrid materials. As shown in Fig. S7a,† the deconvolution peaks of N 1s spectrum of MP-5 were at 399.8 and 401.6 eV, which were assigned to the bonding configuration of the amine (–NH_2) and the protonated amine (–NH_3^+) group, respectively. In contrast, there were no XPS signs corresponding to the oxidizing state of N such as NO_x. Furthermore, we followed the visible absorption of $KMnO_4$ in different systems. As shown in Fig. S7b,† the absorbance at 526 nm of $KMnO_4$ (5 mM) remained unchanged for the pure $KMnO_4$ solution or little changed in the presence of 1 mM I_3K even after 12 hours at room temperature. However, the characteristic absorbance quickly reduced to near zero (typically within 5 minutes) when 10 mM $Mn(NO_3)_2$ was introduced (Fig. S7b†), indicating a rapid reaction between the two kinds of manganese precursors. In the present peptide-directed synthesis of MnO_2, it was thus unlikely that $KMnO_4$ would react with I_3K and instead, it underwent a rapid comproportionation reaction with $Mn(NO_3)_2$, leading to the MnO_2 deposition along the peptide nanofibers.

Therefore, I_3K molecules are suggested to function through self-assembling into nanofibers, which then direct the nucleation and growth of MnO_2. The templating ability of the I_3K nanofibers may arise from the electrostatic attractions between the positively charged groups (–NH_3^+) on their surface and the negatively charged MnO_4^- ions, as well as the interactions (e.g. electrostatic interactions, hydrogen bonding, and van der Waals forces) between the surface groups (–NH_2 and –NH_3^+) and the oligomers of manganese oxides (e.g. tiny nuclei). Portehault et al. have suggested that in the absence of any additives, the growth of MnO_2 during the redox reaction between MnO_4^- and Mn^{2+} could be divided into two stages: in the first stage, the initial reaction between MnO_4^- and Mn^{2+} is too fast to enable the ordered growth and orientation of tiny nuclei, thus leading to the formation of poorly ordered solid spheres, and in the second stage, the slow precipitation kinetics allows the orientated growth of tiny nuclei into small and ultrathin nanoflakes and their subsequent aggregation on the preformed spheres, eventually resulting in the formation of core-corona particles.[35] Here, a similar mechanistic process was proposed for the formation of branched MnO_2 nanowires, as schematically illustrated in Fig. 5. In the presence of the I_3K nanofibers, MnO_4^- ions would be anchored on their surface predominantly via the electrostatic attraction. At first, the disproportion reaction rapidly occurred between Mn^{2+} and the surface-enriched MnO_4^-, resulting in a compact layer of MnO_2 along the peptide nanofibers. Then, the small and ultrathin MnO_2 nanoflakes resulting from the slow reaction between residual Mn^{2+} and MnO_4^- in solution were assembled on the template, eventually leading to the formation of branched MnO_2 nanowires. At low concentrations of manganese precursors, a thin and compact MnO_2 layer along the peptide nanofibers dominated, because nearly all MnO_4^- ions were anchored on the template surface and the nucleation speed was greater than the
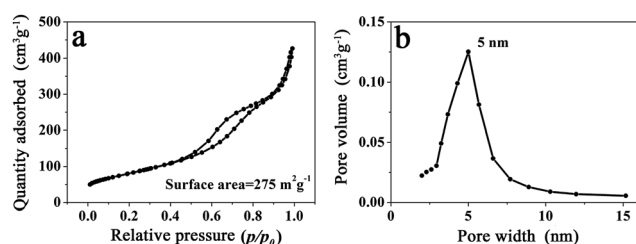

Fig. 4 (a) N_2 adsorption/desorption isotherm and (b) BJH pore size distribution of branched MnO_2 nanowires (MP-5).
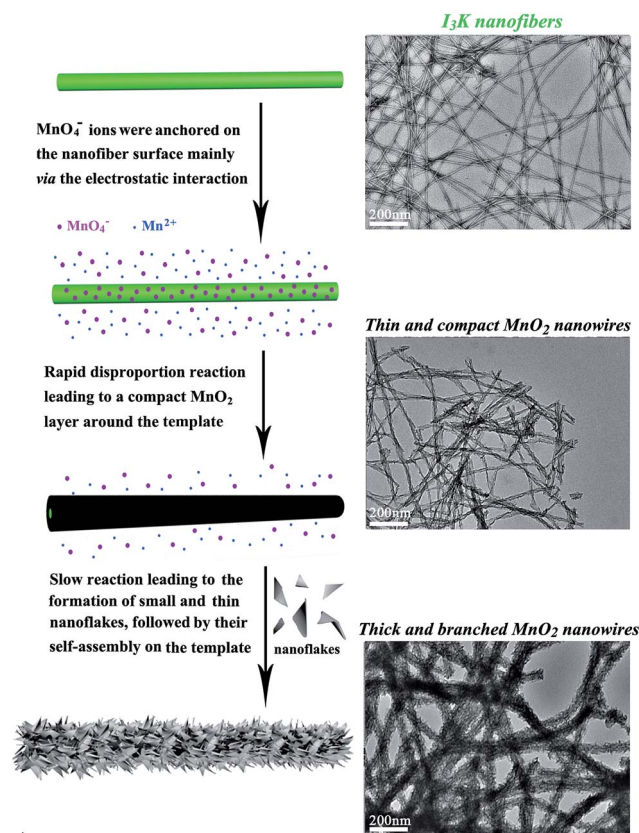
Fig. 5 Schematic illustration of the formation process of branched MnO_2 nanowires directed by the I_3K nanofibers.

growth speed (Fig. 1a). At higher concentrations of manganese precursors, the templating ability of the peptide nanofibers was saturated, eventually leading to the random deposition of urchin-like MnO_2 spheres in addition to branched MnO_2 nanowires (Fig. 1f).

Electrochemical performance of MnO_2 nanostructures

The electrochemical performances of the above MnO_2 nanostructures as the electrode materials for supercapacitors were assessed using the combination of cyclic voltammetry (CV) and galvanostatic charge/discharge techniques. The charge-storage mechanism of MnO_2 is known as the ion coupled redox process: $MnO_2 + Na^+ + e^- \leftrightarrow MnOONa$, which is based on the surface adsorption of electrolyte cations (Na^+) on MnO_2.[2,11,41] Fig. 6a shows the CV curves of the MnO_2 nanomaterials prepared at different precursor concentrations at a scan rate of 5 mV s^{-1}. These CV curves were close to a rectangular shape, being characteristic of pseudocapacitive oxides.[42,43] Furthermore, when the peak current was plotted against the square root of the scan rate in the case of MP-5, a linear relationship was observed between them (Fig. S8†), suggesting a diffusion controlled electrode process.[43–45]

The specific capacitance (C) was calculated from the CV curves according to the following equation:
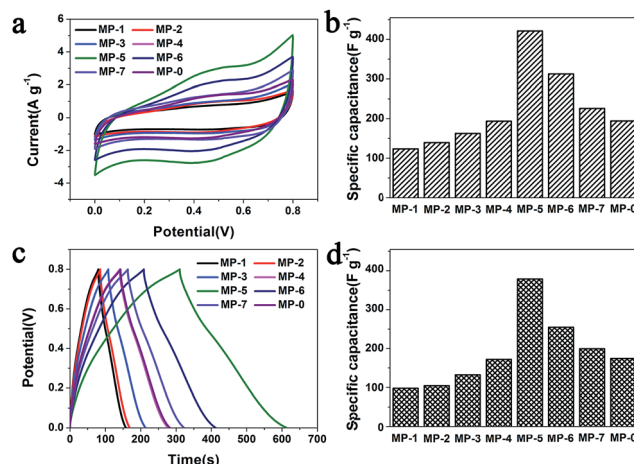

Fig. 6 (a) CV curves of different MnO_2 nanomaterials as the electrode materials in aqueous 1 M Na_2SO_4 at scan rates of 5 mV s^{-1} and (b) the calculated specific capacitances that were calculated according to the eqn (1). (c) Their galvanostatic charge–discharge curves in aqueous 1 M Na_2SO_4 at a current density of 1 A g^{-1} and (d) the specific capacitances that were calculated according to the eqn (2).

$$C = \frac{S}{2m\Delta V \nu} \qquad (1)$$

where S, m, ΔV and ν denote the integral area of the CV curves, the mass of the loaded MnO_2 nanomaterials (including MnO_2 and peptide), the potential window, and the scanning rate, respectively. As shown in Fig. 6b and Table 1, MP-5 showed the largest specific capacitance among the MnO_2 nanostructures. The electrochemical properties of the prepared electrodes were found to be closely related with the content and morphology of MnO_2. The MnO_2/peptide nanowires prepared at low concentrations of manganese precursors (MP-1, MP-2, MP-3, and MP-4) had a compact MnO_2 layer with relatively low MnO_2 contents, thus exhibiting low specific capacitance values. Due to an increase in the relative MnO_2 content in the loaded nanomaterials and the formation of a uniform and loose branched morphology, MP-5 formed at a higher concentration of manganese precursors showed a significantly increased specific capacitance of 421 F g^{-1}. At much higher concentrations of manganese precursors, however, the formed MnO_2 nanomaterials (MP-6 and MP-7) exhibited decreased specific capacitance values, in spite of a further increase in their relative MnO_2 contents. Such a decrease could be ascribed to the occurrence of random urchin-like MnO_2 spheres. In fact, although urchin-like MnO_2 spheres (MP-0) also contained a branched shell consisting of MnO_2 nanoflakes, they showed a clearly decreased specific capacitance relative to the branched MnO_2 hybrid nanowires (MP-5), as shown in Fig. 6b. This can be interpreted that in the latter case, the assembly of MnO_2 nanoflakes along the peptide nanofibers made them well aligned and more loosely packed as well as endowed the formed branched MnO_2 nanowires with a highly porous structure and a large specific surface area. These features not only provided more surface active sites but also favored the transport of electrons and the diffusion of ions, collectively

endowing the branched MnO_2 nanowires with high specific capacitance.

The galvanostatic charge–discharge (GCD) curves at a current density of 1 A g^{-1} for different MnO_2 samples were shown in Fig. 6c. The profiles showed a quasi-linear and symmetric shape, suggesting that all the samples had an excellent reversibility as the electrode materials during the charge/discharge process.[10,37,46,47] The specific capacitance (C) can also be calculated from the GCD curves according to the eqn (2):

$$C = \frac{I\Delta t}{m\Delta V} \qquad (2)$$

where I, Δt, m, and ΔV denote the discharge current, the discharge time, the mass of the loaded MnO_2 nanomaterials (including MnO_2 and peptide), and the potential window, respectively. The results are given in Fig. 6d, which were well consistent with those resulted from the CV curves (Fig. 6b).

In order to test the rate capability and reversibility of the MP-5 electrode, its galvanostatic charge/discharge curves were recorded at different current densities. As shown in Fig. 7a, these almost symmetrical charge/discharge curves indicated an excellent electrochemical reversibility. Furthermore, MP-5 exhibited 63.2% retention of the initial specific capacitance as the current density was increased from 1 to 5 A g^{-1} (Fig. 7b), suggesting a reasonable high-rate capability.[12,37,48] On the other hand, the effect of the scan rate on the capacitance property of MP-5 was also investigated. It could be seen from Fig. S9† that the CV curves remained approximately rectangular at different scan rates and the specific capacitance attained at 234 F g^{-1} even at a high scan rate of 100 mV s^{-1}, demonstrating again a good capacitive property and high-rate capability of MP-5 as the electrode material. These reductions can be ascribed to a decrease in the efficiency of active species at higher current densities or scan rates.[12]

Cycling stability is another crucial parameter for the use of supercapacitors in practical applications. Fig. 7c shows the cycling performance of the electrode prepared from MP-5 nanowires at a scan rate of 5 mV s^{-1} over 2500 cycles. The specific capacitance slightly decreased during cycling and about 93% of the initial capacitance was retained after 2500 cycles. As for the electrode prepared from the urchin-like MnO_2 spheres, approximately 73% of the initial capacitance was kept after 2500 cycles. The results demonstrated an excellent cycling stability of the branched MnO_2 nanowire as the electrode material for supercapacitors. Furthermore, the cycling performance of the MP-5 electrode was also evaluated at varied current densities and the results are shown in Fig. 7d. It can be clearly seen that even suffering from sudden change of the current density, the electrode exhibited stable capacitance, and the specific capacitance at 5 A g^{-1} remained little changed when the current density finally returned to 5 A g^{-1} after a series of varied current densities, indicating again the excellent cycling of MP-5. Although the exact reason for the excellent cycling stability of MP-5 is currently elusive, it is likely related to the morphology of branched nanowires, which can alleviate the aggregation of nanostructures during the charge and discharge process.

Conclusions

By using the I_3K self-assembled nanofibers as the template, MnO_2/hybrid nanowires were synthesized through the comproportionation reaction between $KMnO_4$ and $Mn(NO_3)_2$ in neutral aqueous solution and at room temperature. Because the underlying mechanism was the interaction between the surface-enriched lysine residues of the template and the precursor as well as the oligomers of manganese oxides in solution, the diameter and the surface morphology of the formed MnO_2/hybrid nanowires could be tuned by varying the concentrations of manganese precursors at a fixed peptide concentration. Uniform branched MnO_2/peptide hybrid nanowires (MP-5) were obtained when the concentration of I_3K, $KMnO_4$ and $Mn(NO_3)_2$ was 1, 5, and 10 mM, respectively. The compositional and structural measurements on MP-5 revealed the MnO_2 deposition and the subsequent assembly of small and ultrathin MnO_2 nanoflakes along the peptide nanofibers, thus endowing the well-ordered hybrid sample with high porosity and a large specific surface area of 275 m² g^{-1}. As the electrode materials, the branched MnO_2 hybrid nanowires (MP-5) exhibited excellent supercapacitance performances. Their specific capacitance could attain at a higher value of 421 F g^{-1} and retained about 93% of the initial capacitance after 2500 cycles at a scan rate of 5 mV s^{-1}, and remained little changed during the process of progressively varying the current density. Furthermore, the electrode prepared from MP-5 showed an excellent reversibility and a reasonable high-rate capability during the charge/discharge process. The excellent electrochemical properties of the branched MnO_2 hybrid nanowires arose from their peculiar architecture and properties, including the branched nanowire morphology, higher porosity, and large specific surface area. By taking advantage of peptide self-assembly, the present study demonstrates a potential methodology to prepare MnO_2 nanostructures under mild
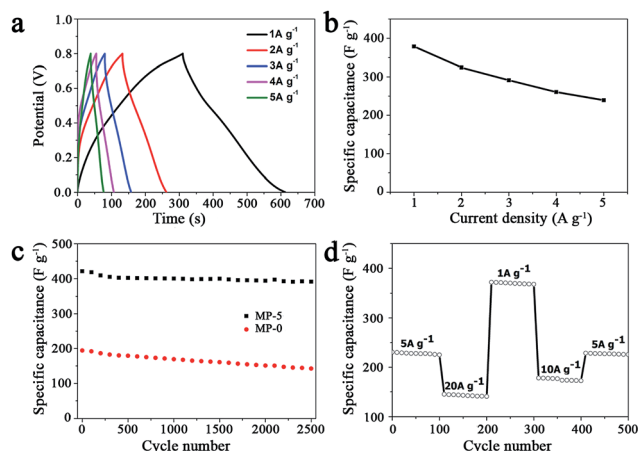

Fig. 7 (a) Galvanostatic charge–discharge curves of MP-5 as the electrode material in aqueous 1 M Na_2SO_4 at different current densities and (b) the variation of the specific capacitances with the current density. (c) Cycling performance of MP-5 as the electrode material in aqueous 1 M Na_2SO_4 at (c) a scan rate of f 5 mV s^{-1} and (d) at progressively varied current densities.

conditions, which possess excellent electrochemical performances as the electrode materials for supercapacitors.

Acknowledgements

Notes and references

1 G. P. Wang, L. Zhang and J. Zhang, *Chem. Soc. Rev.*, 2012, **41**, 797–828.

2 W. Wei, X. Cui, W. Chen and D. G. Ivey, *Chem. Soc. Rev.*, 2011, **40**, 1697–1721.

3 M. Mastragostino, R. Paraventi and A. Zanelli, *J. Electrochem. Soc.*, 2000, **147**, 3167–3170.

4 K. R. Prasad and N. Munichandraiah, *Electrochem. Solid-State Lett.*, 2002, **5**, A271–A274.

5 D. Villers, D. Jobin, C. Soucy, D. Cossement, R. Chahine, L. Breau and D. Bélanger, *J. Electrochem. Soc.*, 2003, **150**, A747–A752.

6 M. J. Young, A. M. Holder, S. M. George and C. B. Musgrave, *Chem. Mater.*, 2015, **27**, 1172–1180.

7 J.-H. Kim, K. Zhu, Y. Yan, C. L. Perkins and A. J. Frank, *Nano Lett.*, 2010, **10**, 4099–4104.

8 C.-C. Hu, K.-H. Chang, M.-C. Lin and Y.-T. Wu, *Nano Lett.*, 2006, **6**, 2690–2695.

9 J. S. Daubert, N. P. Lewis, H. N. Gotsch, J. Z. Mundy, D. N. Monroe, E. C. Dickey, M. D. Losego and G. N. Parsons, *Chem. Mater.*, 2015, **27**, 6524–6534.

10 J. Yan, Z. Fan, T. Wei, W. Qian, M. Zhang and F. Wei, *Carbon*, 2010, **48**, 3825–3833.

11 M. Toupin, T. Brousse and D. Belanger, *Chem. Mater.*, 2004, **16**, 3184–3190.

12 S. Devaraj and N. Munichandraiah, *J. Phys. Chem. C*, 2008, **112**, 4406–4417.

13 P. K. Nayak and N. Munichandraiah, *J. Solid State Electrochem.*, 2012, **16**, 2739–2749.

14 C.-C. Hu, Y.-T. Wu and K.-H. Chang, *Chem. Mater.*, 2008, **20**, 2890–2894.

15 V. Subramanian, H. Zhu, R. Vajtai, P. M. Ajayan and B. Wei, *J. Phys. Chem. B*, 2005, **109**, 20207–20214.

16 S. Zhao, T. Liu, D. Hou, W. Zeng, B. Miao, S. Hussain, X. Peng and M. S. Javed, *Appl. Surf. Sci.*, 2015, **356**, 259–265.

17 A. Sarkar, A. K. Satpati, V. Kumar and S. Kumar, *Electrochim. Acta*, 2015, **167**, 126–131.

18 G. Qiu, H. Huang, S. Dharmarathna, E. Benbow, L. Stafford and S. L. Suib, *Chem. Mater.*, 2011, **23**, 3892–3901.

19 J.-K. Chang and W.-T. Tsai, *J. Electrochem. Soc.*, 2003, **150**, A1333–A1338.

20 Q. Li, X.-F. Lu, H. Xu, Y.-X. Tong and G.-R. Li, *ACS Appl. Mater. Interfaces*, 2014, **6**, 2726–2733.

21 M. B. Dickerson, K. H. Sandhage and R. R. Naik, *Chem. Rev.*, 2008, **108**, 4935–4978.

22 S. Wang, Q. Cai, M. Du, J. Xue and H. Xu, *J. Phys. Chem. B*, 2015, **119**, 12059–12065.

23 H. Xu, Y. Wang, X. Ge, S. Han, S. Wang, P. Zhou, H. Shan, X. Zhao and J. R. Lu, *Chem. Mater.*, 2010, **22**, 5165.

24 S. Han, S. Cao, Y. Wang, J. Wang, D. Xia, H. Xu, X. Zhao and J. R. Lu, *Chem.–Eur. J.*, 2011, **17**, 13095.

25 S. Wang, X. Ge, J. Xue, H. Fan, L. Mu, Y. Li, H. Xu and J. R. Lu, *Chem. Mater.*, 2011, **23**, 2466–2474.

26 S. Wang, J. Xue, X. Ge, H. Fan, H. Xu and J. R. Lu, *Chem. Commun.*, 2012, **48**, 9415–9417.

27 D. P. Dubal, D. Aradilla, G. Bidan, P. Gentile, T. J. S. Schubert, J. Wimberg, S. Sadki and P. Gomez-Romero, *Sci. Rep.*, 2015, **5**, 9771, DOI: 10.1038/srep09771.

28 B. Li, G. Rong, Y. Xie, L. Huang and C. Feng, *Inorg. Chem.*, 2006, **45**, 6404–6410.

29 J. Yan, Z. Fan, T. Wei, J. Cheng, B. Shao, K. Wang, L. Song and M. Zhang, *J. Power Sources*, 2009, **194**, 1202–1207.

30 H. Xia, M. Lai and L. Lu, *J. Mater. Chem.*, 2010, **20**, 6896–6902.

31 Z. Li, Y. Mi, X. Liu, S. Liu, S. Yang and J. Wang, *J. Mater. Chem.*, 2011, **21**, 14706–14711.

32 Z. Li, J. Wang, S. Liu, X. Liu and S. Yang, *J. Power Sources*, 2011, **196**, 8160–8165.

33 M. Chigane and M. Ishikawa, *J. Electrochem. Soc.*, 2000, **147**, 2246–2251.

34 H. W. Nesbitt and D. Banerjee, *Am. Mineral.*, 1998, **83**, 305–315.

35 D. Portehault, S. Cassaignon, N. Nassif, E. Baudrin and J.-P. Jolivet, *Angew. Chem., Int. Ed.*, 2008, **47**, 6441–6444.

36 L. Yu, G. Zhang, C. Yuan and X. W. Lou, *Chem. Commun.*, 2013, **49**, 137–139.

37 H. Zheng, J. Wang and C. Ma, *J. Power Sources*, 2012, **216**, 508–514.

38 Y. Chen, B. Xie, S. Luo and Y. Zhang, *Appl. Surf. Sci.*, 2013, **285P**, 425–430.

39 J. Li, N. Wang, Y. Zhao, Y. Ding and L. Guan, *Electrochem. Commun.*, 2011, **13**, 698–700.

40 S.-B. Ma, K.-Y. Ahn, E.-S. Lee, K.-H. Oh and K.-B. Kim, *Carbon*, 2007, **45**, 375–382.

41 D. Bélanger, T. Brousse and J. W. Long, *Electrochem. Soc. Interface*, 2008, **17**, 49–52.

42 T. Brousse, D. Bélanger and J. W. Long, *J. Electrochem. Soc.*, 2015, **162**, A5185–A5189.

43 B. E. Conway, *Electrochemical supercapacitors: scientific fundamentals and technological applications*, Kluwer Academic/Plenum Press, New York, 1999.

44 P. Simon, Y. Gogotsi and B. Dunn, *Science*, 2014, **343**, 1210–1211.

45 R. N. Reddy and R. G. Reddy, *J. Power Sources*, 2004, **132**, 315–320.

46 Y.-C. Chen, Y.-K. Hsu, Y.-G. Lin, Y.-K. Lin, Y.-Y. Horng, L.-C. Chen and K.-H. Chen, *Electrochim. Acta*, 2011, **56**, 7124–7130.

47 S. Chen, J. Zhu, X. Wu, Q. Han and X. Wang, *ACS Nano*, 2010, **4**, 2822–2830.

48 J. Liu, J. Jiang, C. Cheng, H. Li, J. Zhang, H. Gong and H. J. Fan, *Adv. Mater.*, 2011, **23**, 2076–2081.